Numerical Simulation of Hindered Diffusion in γ-Alumina Catalyst Supports

Haisheng Wang, François Willot, Maxime Moreaud, Mickaël Rivallan, Loïc Sorbier, Dominique Jeulin

Oil & Gas Science and Technology – Rev. IFP Energies nouvelles (2017) **72**, 8

DOI: 10.2516/ogst/2017002

Numerical Simulation of Hindered Diffusion in γ-Alumina Catalyst Supports

Haisheng Wang[1], François Willot[1]*, Maxime Moreaud[2], Mickaël Rivallan[2], Loïc Sorbier[2] and Dominique Jeulin[1]

[1] MINES ParisTech, PSL - Research University, CMM - Centre for Mathematical Morphology, 35 rue Saint Honoré, 77300 Fontainebleau Cedex - France

[2] IFP Energies nouvelles, Rond-point de l'échangeur de Solaize, BP 3, 69360 Solaize - France

e-mail: haisheng.wang@mines-paristech.fr - francois.willot@mines-paristech.fr - maxime.moreaud@ifpen.fr - mickael.rivallan@ifpen.fr - loic.sorbier@ifpen.fr - dominique.jeulin@mines-paristech.fr

* Corresponding author

Abstract *— By employing multi-scale random models of γ-alumina, we have studied the influence of porosity, grain aspect ratio and aggregation state on the effective diffusion coefficient. Multi-scale Boolean models of platelets were used to produce digital volumes reproducing the alumina porous space. Iterative fast Fourier transform numerical simulation of Fick's diffusion were performed on the volume to obtain the effective diffusion coefficient. The tortuosity factors of the various simulated models show a simple dependence with pore volume fraction with an exponent guided by the platelet aspect ratio and the aggregation state. Comparisons with proton pulsed-field gradient nuclear magnetic resonance spectrometry show a satisfactory agreement.*

Résumé — Simulation numérique de la diffusion restreinte dans les supports de catalyseurs d'alumine γ — Nous avons étudié l'influence de la porosité, du facteur d'allongement des grains et de l'état d'aggrégation sur le coefficient de diffusion effectif à l'aide de modèles aléatoires multi-échelles d'alumine γ. Des schémas Booléens multi-échelles ont été utilisés pour obtenir des volumes numériques représentant l'espace poral des alumines. Des simulations numériques de diffusion de Fick utilisant des itérations de transformées de Fourier rapides ont été réalisées sur les volumes afin d'obtenir les coefficients de diffusion effectifs. La tortuosité des différents modèles suit une loi fonction de la porosité, avec un exposant dépendant de l'allongement des plaquettes et de l'état d'aggrégation. Des comparaisons avec des mesures de spectrométrie de résonance magnétique nucléaire du proton à gradient de champ pulsé montrent un accord satisfaisant.

INTRODUCTION

Porous γ-alumina is a widely used support for heterogeneous catalysts in the refining and petrochemical industry. The mass transport property in nanoporous solid is driven by diffusion. Among important industrial processes under internal diffusional limitation, one finds hydrodemetalation of vacuum residues [1], fixed-bed Fischer-Tropsch synthesis [2] and selective hydrogenation of unsaturated hydrocarbons [3, 4]. For these processes, diffusion at the catalyst pellet's scale occurs at a lower pace than the chemical reaction, leading to internal diffusional limitations. Increasing the diffusion efficiency may lead to increased catalyst efficiency and overall process conversion.

Mass transport of liquids in nanoporous media is a complex process, where hindered diffusion dominates. Hindered diffusion occurs when the gyration radius of the diffusing molecule is not negligible compared to the size of the pores. The ratio λ of the gyration radius r_g of the molecule to the pore radius r_p plays an important role:

$$\lambda = \frac{r_g}{r_p} \tag{1}$$

Liquid diffusion in nanoporous media occurs at a slower pace than in bulk liquids. The effective diffusion coefficient D_e reads [5]:

$$D_e = \frac{\varepsilon K_p(\lambda) K_d(\lambda)}{\tau(\lambda)} D_0 \tag{2}$$

where D_0 is the molecular diffusion coefficient, ε the pore volume fraction, τ the tortuosity factor, K_p the partition coefficient, and K_d the drag coefficient. Three phenomena which slow down mass transport have been taken into account in the equation:

- the tortuosity of the porous space, implying that a molecule has to travel a longer path than the Euclidean distance to move from two remote (far away as compared to the pore size) points. This effect is described by a tortuosity factor τ;
- the steric hindrance, which describes the fact that a finite size molecule cannot approach more than its gyration radius to the pore walls. This effect is described by a partition coefficient K_p;
- a difference in viscous drag of the molecule due to the vicinity of the pore walls, modeled by a drag coefficient K_d.

For molecules much smaller than the pore size, $K_p = K_d = 1$. For a cylindrical pore, a molecule having a giration radius r_g has access to a fraction of the pores equal to $K_p\varepsilon$, where:

$$K_p = (1 - \lambda)^2 \tag{3}$$

Several expressions have been proposed for the K_d factor depending on the geometry and method of averaging [6, 7]. The most employed factor, called the Renkin's equation, has been computed for a geometry made of a hard sphere in a cylindrical pore and reads, for $0 \leq \lambda \leq 0.4$:

$$K_d = 1 - 2.1044\lambda + 2.089\lambda^3 - 0.948\lambda^5 \tag{4}$$

For rather small molecules, an empirical formula has been proposed in [8]:

$$K_d K_p = \exp(-2\lambda) \tag{5}$$

The tortuosity factor τ strongly depends on pore space topology and porosity. A general relation between τ and ε in the high porosity regime was proposed in [9]:

$$\tau = 1 - p \ln \varepsilon \tag{6}$$

where p is specific to the pore space topology, hence to the geometry of particles forming the solid. Equation (6) with $p = 0.5$ is an upper bound of the effective diffusion coefficient in a random model of overlapping sphere [10]. Its applicability has been experimentally assessed by permeability [9], electrical conductivity [11] or effective diffusion [5] measurements.

Hindered diffusion coefficient in nanoporous solids can be measured by proton Pulsed-Field Gradient Nuclear Magnetic Resonance (PFG-NMR) [12], inverse chromatography [5], membrane permeation or modeling of the kinetics of adsorption of the solute in a batch reactor [13, 14]. It is worth mentioning that PFG-NMR measures a self-diffusion coefficient, and the measurement is done only in the part of the pore space that is accessible by the probe molecule. However, the fluids in the pores are influenced by an apparent change of viscosity compared to the free fluid, therefore the viscous drag factor is kept in Equation (7). Then, the confined diffusion coefficient probed by Nuclear Magnetic Resonance (NMR) D_e^{NMR} is related to the molecular diffusion coefficient D_0^{NMR} by:

$$D_e^{NMR} = \frac{K_d(\lambda)}{\tau(\lambda)} D_0^{NMR} \tag{7}$$

PFG-NMR is well established to measure effective self-diffusion coefficient in porous media. Proton spins are phase-encoded and decoded by a field gradient impulsion and attenuation of the NMR signal can be related to the effective diffusion coefficient. Indeed, PFG-NMR allows to map the diffusion propagator in q space, the magnetization wave vector [15]. Assuming long diffusion times Δ and a small magnetization wave vector q, the propagator is Gaussian and there is a simple relation between the ratio of echo intensities $S(g)$ with a field gradient over $S(0)$ without gradient, the parameters of the NMR sequence and the confined diffusion coefficient D_e^{NMR}. Using the stimulated echo sequence proposed by [16], this relation writes:

$$\ln\left(\frac{S(g)}{S(0)}\right) = -D_e^{NMR}\gamma^2 g^2 \delta^2 \left(\Delta - \frac{\delta}{3}\right) \tag{8}$$

where γ is the gyromagnetic ratio of the probed nucleus, g is the intensity of the field gradient pulses, δ is the duration of the gradient pulses and Δ the time between the two gradient

pulses (diffusion time). In this case, if $\delta \ll \Delta$ the magnitude of magnetization wave vector q is:

$$q = \gamma g \delta \tag{9}$$

Following the argument of Callaghan *et al.* [15], effective diffusion measurement by PFG-NMR must be performed in the regime $1/q \gg d_p$, where d_p is the pore diameter.

PFG-NMR has been used to study the diffusion of probe molecules in various mesoporous samples: water in silica and alumina [12] or in mesoporous NaA zeolite [17], *n*-pentane and *n*-heptane in alumina and used hydroprocessing catalysts [18], *n*-octane and 1,3,5-triisopropylbenzene in mesoporous Y zeolithe [19] or *n*-hexane in micro-mesoporous activated carbon [20]. Hollewand and Gladden found a D_0^{NMR}/D_e^{NMR} ratio equal to 1.8 for water diffusing in a 182 m^2/g specific surface area alumina support [12]. Wood and Gladden have observed such ratio equal to 1.6 and 2.37 respectively for pentane and heptane in a 372 m^2/g specific surface area alumina support [18]. DOSY (Diffusion Ordered SpectroscopY) is a class of NMR sequences that allows the simultaneous measurement of the classical NMR spectrum (chemical shift) with the measurement of the apparent diffusion coefficient [21-23]. The Fourier transform of the free induced decay signal gives the NMR spectrum whereas the inverse Laplace transform of the echo attenuation yields the apparent diffusion coefficient [15, 24]. DOSY allows determination of diffusion coefficient of molecules with close chemical shifts, ideal for the studies of complex mixtures and oil products [25].

Self-diffusion coefficient in pure toluene measured by PFG-NMR can be found in literature. Extrapolated values at 295 K found are 2.11 [26], 2.22 [27] and 2.39×10^{-9} m^2/s [28]. Using the value of viscosity η = 575.3 µPa s [29] and $D_0 = 2.39 \times 10^{-9}$ m^2/s the Stokes-Einstein formula gives an hydrodynamic radius r_g = 0.16 nm at 295 K.

Some works focused on the simulation of transport in porous media. They differ in the class of model used for generating the porous space and the homogenization methodology, the way to obtain the effective diffusion coefficient. The different classes of models encountered in the literature may be sorted in the following categories [30, 31]:

- parallel bundles of cylindrical or slit-shaped pores;
- process-based models where the pore space is obtained by mimicking the genesis of the solid [32-34];
- grain models where point statistics are reproduced using simulated annealing [35, 36];
- random sets [37];
- random Gaussian fields [38-40];
- networks of pores [41];
- fractal models [42].

γ-alumina pore space morphology is the result of the aggregation of individual platelets [43] and is then better modeled by approaches keeping the geometry of the grains such as process-based or random sets models. Platelet shape is expected to be an octagonal prism from density functional theory computation [44]. Typical sizes of platelets reported in the literature are in the 1 nm to 1 µm range with an aspect ratio in the range 1 to 100 [45-50]. Generally, several scales of aggregation are encountered: the platelets are packed in aggregates that generates a small-sized mesoporosity [43]. The packing of aggregates produces itself a large-sized mesoporosity. Multi-scale random sets models can be tuned to reproduce porosimetry measurements and Transmission Electron Microscopy (TEM) images of real samples [51]. The use of at least two aggregation scales is mandatory to reproduce accurately second order statistics [51].

Homogenization of diffusion process may be performed by different methods:

- Brownian dynamics whose principle is to follow individual molecule trajectories paths by Monte Carlo simulations and retrieve their mean square displacement to compute D_e [32];
- finite element method where Fick's equation is solved in the porous space [52];
- iterative Fast Fourier Transform (FFT) scheme where Fick's equation is solved through a Lippmann-Schwinger equation [53, 54]. This method is particularly well suited if the porous space is digitalized.

The aim of this paper is to explore the influence of platelet morphology and aggregation state on the transport properties of γ-alumina with the help of random sets models. The effective diffusion coefficient is obtained from digital realizations of the random sets using an iterative FFT scheme. Simulated effective diffusion coefficient is compared to PFG-NMR measurement on representative alumina. In the next section, we present the methodologies for generating random models of platelets reproducing the morphology of γ-alumina for the homogenization problem, and gives samples characteristics and measurement method for PFG-NMR. Results are given in the next section, followed by a general discussion, conclusion and perspectives of this work.

1 MATERIALS AND METHODS

1.1 Random Models of γ-Alumina

A two-scale random model of platelets, proposed in a previous work [51] based on TEM images of mesoporous alumina, is generated by following procedure:

1. A Boolean model of spheres of fixed diameter, each sphere assigned with a random orientation uniformly sampled on the unit sphere;

2. Two Poisson point processes with two different densities are generated inside and outside the spheres;
3. A platelet with a fixed shape is located at each Poisson point. The platelet has a random direction if the point is outside the sphere. It has the direction assigned to the sphere if the point is inside a sphere. If the point belongs to several spheres, the platelet direction is chosen randomly between the directions assigned to the spheres.

Such a model has eight parameters, four defining the shape of the platelets (Fig. 1) and four controlling the aggregation state: the sphere radius r_S, the volume fraction of spheres p_S, the volume fraction of platelets in the spheres p_A and the volume fraction of platelets outside the spheres p_B. The four latter parameters are related with the porosity ε by:

$$p_B(1-p_S)+p_A p_S \approx 1-\varepsilon \tag{10}$$

Parameters of the model were identified from TEM images of sliced sample of each alumina using the correlation function in [51].

The identification is made by an inverse problem approach with L2-norm minimization and considering high frequencies as noise added to the model, which leads to the underestimation of the platelet size. To better identify the two-scale model, the noise background is accordingly added in the simulation of TEM images (as shown in Fig. 2). The parameters identified using the correlation function of simulated TEM images are shown in Table 5 (last row). The model is validated by specific surface area (Tab. 1) measured by nitrogen porosimetry. The platelet size and shape are in agreement with TEM image observations and with literature [45]. A 3D realization of the identified two-scale model is shown in Figure 3.

For comparison with PFG-NMR measurement on the diffusion property, this newly identified two-scale model of mesoporous alumina is used in Section 2.5.

1.2 Estimation of the Effective Diffusion Coefficient

1.2.1 Fick's Diffusion

The steady-state diffusion governed by the Fick's first law is considered. Let $\boldsymbol{J}_i(\mathbf{r})$ be the diffusion flux of molecules along the i axis and $c(\mathbf{r})$ the concentration of molecule at point $\mathbf{r}$, the Fick diffusion equation reads, in the permanent regime (time-independent):

$$\begin{cases} J_i(\mathbf{r}) = -D(\mathbf{r})\partial_i c(\mathbf{r}) \\ \partial_i J_i(\mathbf{r}) = 0 \end{cases} \tag{11}$$

where $D(\mathbf{r})$ is the local diffusion coefficient. The effective diffusion coefficient $\mathbf{D}_e$ of the porous medium is defined by:

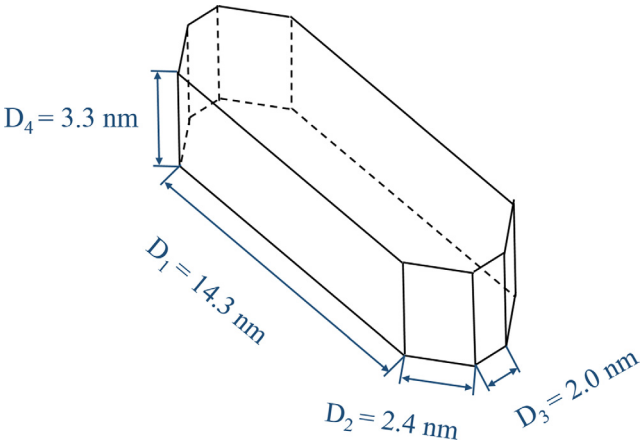

Figure 1

Prism shape of γ-alumina grain identified with the TEM images of sample 1.

$$\langle J_i \rangle = (\mathbf{D}_e)_{ij}\langle -\partial_j c \rangle. \tag{12}$$

where $\langle\cdot\rangle$ stands for volume averaging. Hereafter, we assume that the microstructure is statistically isotropic and identify D_e with a scalar.

1.2.2 Analytical Bounds and Estimates

The Hashin-Shtrikman lower bound for the effective diffusion coefficient of a porous medium is zero. For 3D media, the upper bound is [55]:

$$D_e \le \mathrm{D}_{\max}^{\mathrm{HS}} = D_0\left(\frac{2\varepsilon}{3-\varepsilon}\right). \tag{13}$$

1.2.3 Numerical Computation: FFT-Fick Diffusion

We use an auxiliary field $\mathbf{E} = -\nabla \mathrm{c}$ and note that the problem of Fick diffusion is mathematically (not physically) equivalent to that of electrical response of materials [54]. According to this analogy, diffusion flux is associated with electrical current, the concentration gradient to electric field, concentration to electric potential and diffusion coefficient to conductivity. We now consider a three-dimensional cubic domain $\Omega = [-L/2, L/2]^3$ of width L. The edges of the domain are aligned with the Cartesian unit vectors $\mathbf{e}_i$ with $i \in \{1, 2, 3\}$ and periodic boundary conditions are employed:

$$\mathbf{J}(\mathbf{r})\cdot\mathbf{n} - \#, \quad c(\mathbf{r}+L\mathbf{e}_i) \equiv c(\mathbf{r}) - \overline{E}_i L, \quad \mathbf{r}, \mathbf{r}+L\mathbf{e}_i \in \partial\Omega \tag{14}$$

where $-\#$ means anti-periodicity, $\mathbf{n}$ is the outer normal of $\partial\Omega$, and $\overline{\mathbf{E}}$ is an applied concentration gradient.

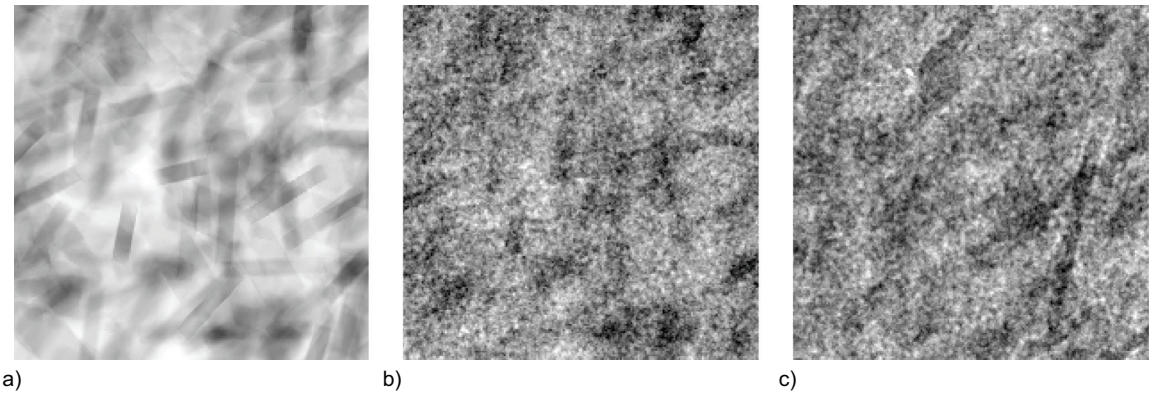

Figure 2

Comparison between the textures of a) a 2D projection of a 3D simulation of microstructure formed with platelets, b) a simulated TEM image based on the 2D projection with background noise, and c) an experimental TEM image of sample 2. The microstructure volume is $65 \times 65 \times 70$ nm^3, where 70 nm is the thickness along the projection direction.

TABLE 1

Texture characterization of alumina samples. The value of λ is estimated using the average median pore diameter $d_p = \left(d_p^{Hg} + d_p^{BJH}\right)/2$. The coefficients K_d and K_p are calculated with Equations (4) and (3) respectively. The accessible pore volume fraction ε_t is estimated by εK_p.

Sample	S_{BET} m^2/g	ε	d_p (Hg) nm	d_p (BJH) nm	ε_t	λ 10^{-2}	K_p	K_d
Sample 1	240	0.69	11.3	12.9	0.68	2.64	0.948	0.944
Sample 2	223	0.71	10.7	15.7	0.70	2.42	0.952	0.949
Sample 3	247	0.73	10.7	15.9	0.72	2.41	0.953	0.949

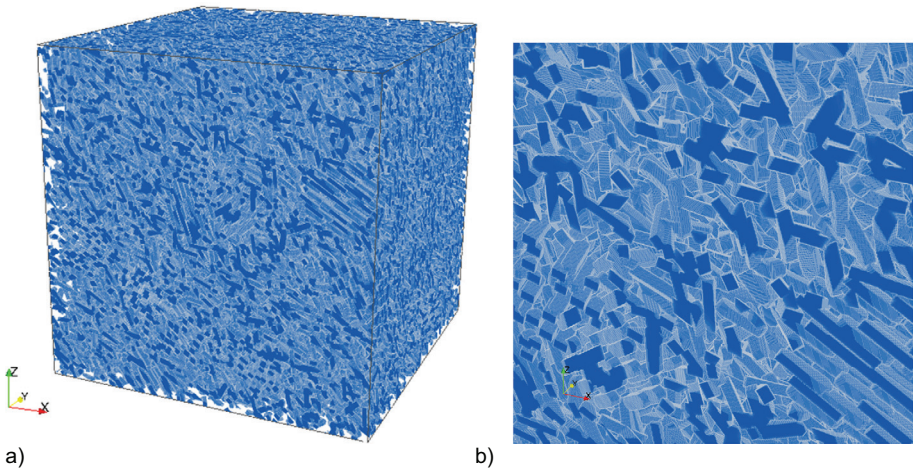

Figure 3

3D simulation of the microstructure of mesoporous alumina with the two-scale model of platelets identified with TEM images and specific surface area. The total number of implanted platelets in the microstructure is 63 506, including 12 141 aligned platelets and 51 365 randomly-oriented platelets. The parameters of the model are given in Table 5 (last row). a) $300 \times 300 \times 300$ nm^3, b) zoom in with field of view about 50×50 nm^2.

To apply FFT methods, we rewrite Equation (11) as the Lippmann-Schwinger's equation [53]:

$$\begin{cases} E_i = \overline{E_i} - \tilde{G}_{i,j} * P_j \\ P_j = J_j - \tilde{D} E_j \end{cases} \quad (15)$$

where $\tilde{D}$ is an arbitrary reference diffusion coefficient, **P** is the associated polarization field, $\tilde{G}$ the Green operator and * the convolution product. The convolution product in Equation (15) may be advantageously evaluated in the Fourier domain. FFT methods consist in iterating the following equation until convergence:

$$\mathbf{E}^{m+1} = \overline{\mathbf{E}} - \tilde{G} * \left[(D - \tilde{D}) \mathbf{E}^m \right] \quad (16)$$

where $\mathbf{E}^m$ is the opposite of the concentration gradient at iteration m.

The effective diffusion coefficient D_e is obtained from the flux passing through a face S_i normal to the i axis:

$$D_e = \frac{\iint_{S_i} D(\mathbf{r}) E_i(\mathbf{r}) \mathrm{d}r_j \mathrm{d}r_k}{L^2 \overline{E}_i} \quad (17)$$

where $-\overline{E}_i$ is the applied (macroscopic) concentration gradient along axis i, r_j and r_k are the Cartesian coordinates along the other two axis.

1.3 Alumina Samples

Three mesoporous alumina were synthesized from different commercial boehmite powders and from solution of aluminium nitrate and sodium aluminate. They are expected to have different nano-particle shapes. The three alumina are shaped in the form of cylindrical extrudates of 1.3 mm diameter. All samples are translucent indicating a weak diffusion by visible light and consequently no important structural heterogeneity above visible light wavelength (hundredth of nm). Specific surface area S_{BET} (in m^2/g) was measured by nitrogen adsorption with the Brunauer-Emmett-Teller (BET) method [56]. Extrudates are pretreated at 623 K for 3 h under vacuum (10^{-4} Pa) before measurement. Structural density ρ_s (in g cm^{-3}) was measured by He pycnometry after a pretreatment (523 K for 3 h). Grain density ρ_g (in g cm^{-3}) was measured by mercury intrusion after a pretreatment (523 K for 2 h). The grain density is obtained at a 0.2 MPa intrusion pressure where mercury fills only intergrain porosity but not intragrain porosity. The porosity ε (void volume fraction) is obtained from:

$$\varepsilon = 1 - \frac{\rho_g}{\rho_s} \quad (18)$$

Median pore diameter d_p is defined as the diameter where half of the mesoporous volume is contained in pores bigger and smaller than d_p. It was obtained from mercury intrusion and the Barrett-Joyner-Halenda (BJH) calculation of the desorption branch of nitrogen porosimetry. The accessible pores by toluene is calculated by:

$$\varepsilon_t = \varepsilon K_p(\lambda) \quad (19)$$

where $K_p(\lambda)$ is estimated from Equation (3) using the hydrodynamic radius of toluene and the median pore radius (Tab. 1).

1.4 PFG-NMR Measurements

About 15 extrudates are placed in a 5 mm diameter tube and immersed in 10% deuterated toluene. The deuterated fraction has the purpose of locking the NMR probe on the deuterium resonance frequency. Measurements were performed with a Bruker Avance 600 spectrometer (600 MHz resonance frequency for proton). Temperature is controlled during the experiments at 295 K. Longitudinal relaxation time T_1 is measured by inversion-recovery sequence and transverse relaxation time T_2 by Carr-Purcell-Meiboom-Gill (CPMG) sequence. The relaxation time measurement is mandatory to optimize delay parameters included in the DOSY experiments.

The echo attenuation coefficients are measured using the Bipolar Pulse Pairs Longitudinal-Eddy-current Delay STimulated Echo (BPP-LED-STE) sequence with parameters δ = 2.5 ms, Δ = 140 ms and τ = 0.05 µs [57]. q space is probed by varying the intensity of the gradient g (from 6.81×10^{-3} Tm^{-1} to 3.24×10^{-1} Tm^{-1}), in order to obtain 16 values of attenuation from 2 to 95%. The values of the parameters are consistent with the small q requirement as $\left(\frac{1}{q}\right)_{\min} = 2.9 \times 10^4$ nm. Data are processed by the software Dynamics Center 2.3.1 from Bruker. Both free D_0^{NMR} and confined D_e^{NMR} toluene diffusion coefficients are measured after data processing of the DOSY experiment. From the experimental data, the tortuosity factor τ is estimated by Equation (7). Following the expressions of Equations (2) and (7), the effective diffusion coefficient D^e is obtained by:

$$D_e = \frac{\varepsilon_t D_e^{NMR}}{D_0^{NMR}} D_0 \quad (20)$$

where D_0 is the free toluene diffusion coefficient obtained by a reference DOSY measurement performed on a tube filled with only 10% vol. deuterated toluene at 295 K.

TABLE 2
Experimental values from T_1 and T_2 relaxation measurements of toluene molecule (10% vol. deuterated) at 295 K.

Sample preparation	Molecule	T_1 (ms)	T_2 (ms)	T_1/T_2
Toluene	Toluene free molecule	4790	2440	2.0
Toluene + alumina extrudate	Toluene free molecule	4850	1390	3.5
Toluene + alumina extrudate	Confined toluene	1900	116	16.4

For comparison between experiments and simulations, we use the formation factor [58] as benchmark, defined as the ratio of free to confined diffusion coefficients:

$$F = \frac{D_0}{D_e} \tag{21}$$

2 RESULTS

2.1 Texture of Alumina

Results of texture characterization, measured from mercury intrusion and nitrogen porosimetry, are summarized in Table 1.

The three alumina have close textural properties. As toluene has a small hydrodynamic radius compared to the mean pore size, most pores are accessible by toluene. Nitrogen desorption and mercury intrusion give different values for the median pore diameter but after averaging it does not appreciably change the obtained K_p value and hence the accessible porosity by toluene.

2.2 Effective Diffusion from PFG-NMR

The values of relaxation times of toluene in presence of alumina extrudates are reported in Table 2.

DOSY spectra of pure toluene and alumina plunged into toluene are shown in Figure 4. For free toluene (Fig. 4a), the five protons of the aromatic cycle are observed between 7 and 8 ppm, whereas the three protons of the methyl group are observed between 2 and 2.5 ppm. The 5/3 expected ratio of the peaks area is correctly recovered. A single diffusion coefficient is observed $D_0 = 2.40 \times 10^{-9}$ m^2/s, compatible with the value found in literature. For toluene in all alumina, a strong broadening of both aromatic and methyl proton peaks is observed. Chemical shifts of confined toluene protons are shifted to higher values. Two distinct diffusion coefficients for free and confined toluene are systematically observed. NMR signal attenuation is linear at small gradient (Fig. 5) which is compatible with a Gaussian propagator and then to a Fick's law [59]. This justifies the homogenization approach with a Fick formalism employed in this work. Numerical values of the diffusion coefficient extracted from DOSY spectra are reported in Table 3. As expected by the subtle variation in texture, the effective diffusion coefficients of the three alumina are found very close. It should be noticed that the range of diffusion coefficients of free toluene from the three alumina is much greater than the uncertainty of measurement in pure toluene.

2.3 Effects of Particle Shape on Effective Diffusion

In order to study the effects of particle shape on the effective diffusion coefficient, Boolean models of prisms are considered, to generate virtual materials. Prism morphology is deduced from XRD experiments [45] on boehmite nanoparticles, which is the topotactic precursor of γ-alumina. The influence of platelet aspect ratio is studied by keeping a constant volume for the platelet but taking a cubic shape ($4 \times 4 \times 4$ nm), a platelet-like shape ($7.1 \times 3 \times 3$ nm) and a rod-like shape ($16 \times 2 \times 2$ nm) in length $\times$ width $\times$ height. A Boolean model of spheres plays the role of reference with radius 2.5 nm. The volume fraction of pores is fixed to 70%. Orientations of the platelets in simulated 3D microstructures are isotropic. The microstructure volume is $300 \times 300 \times 300$ nm^3 (909^3 voxels at resolution 0.33 nm per voxel).

A macroscopic concentration gradient is applied between the two faces along the first axis: $\overline{\mathbf{E}} = (1, 0, 0)$. The diffusion flux in the porous phase is numerically computed with the FFT-Fick diffusion method. After the algorithm has converged, the steady concentration field is obtained, together with the flux field. 2D sections of the first component of the flux fields J_1 are shown in Figure 6.

The effective diffusion coefficients D_e of the four Boolean models of spheres, cubic prisms, platelet-like prisms and rod-like prisms, denoted by D_e^S, D_e^C, D_e^P and D_e^R respectively, are estimated by averaging over the flux field $\langle J_1 \rangle$ (shown in Tab. 4; Fig. 7). The relative error on the predicted macroscopic properties is given by $e_r = 2\sqrt{D^2(V_0)}/\langle J_1 \rangle$ where V_0 is the volume of the microstructure and $D^2(V_0)$ is the

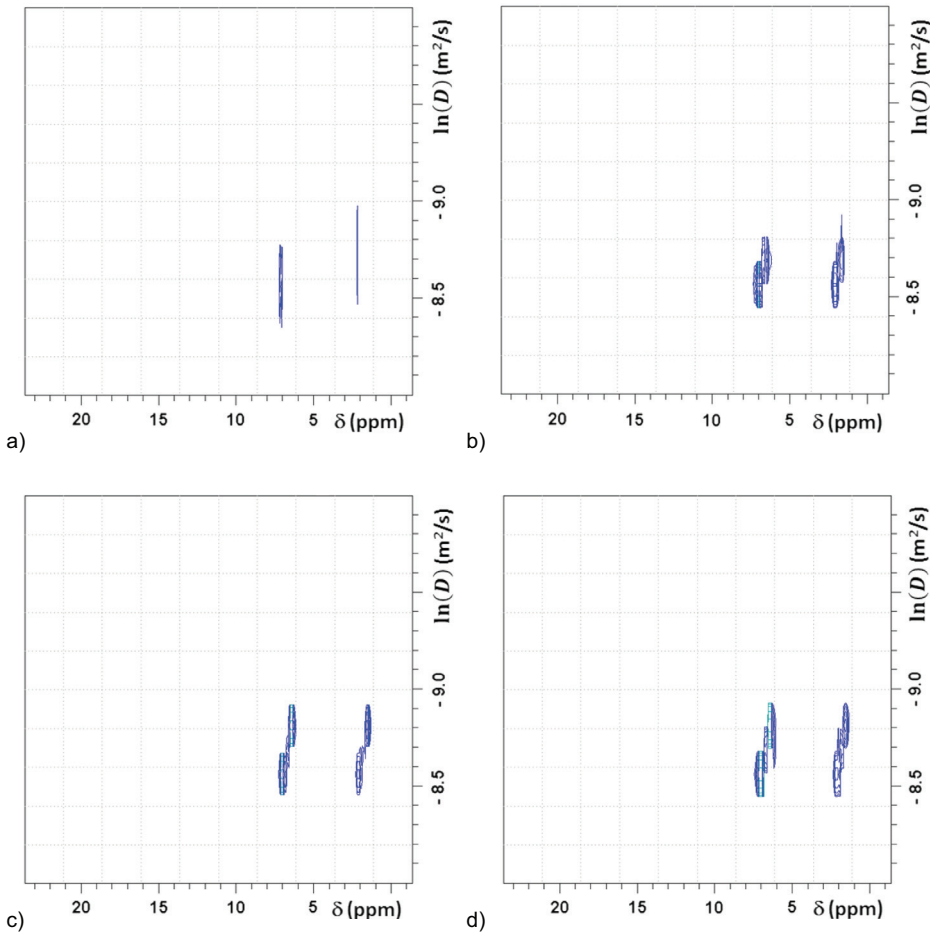

Figure 4

DOSY spectra of pure toluene and toluene in alumina. The horizontal axis is the NMR chemical shift in part per million. The vertical axis is the logarithm of diffusion coefficient in m^2/s. a) toluene, b) alumina sample 1, c) alumina sample 2, d) alumina sample 3.

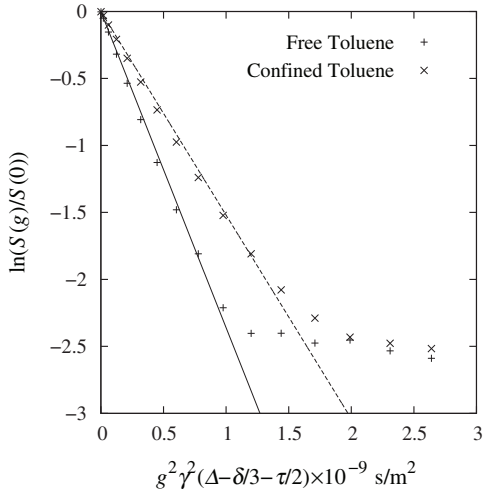

Figure 5

PFG-NMR signal attenuation of aliphatic protons of free and confined toluene for sample 1. Lines are linear fit on first 8 points.

variance of $\langle J_1 \rangle$ on domains of size V_0. The latter is estimated by computing the apparent properties of independent realizations of size V_0. For the four considered models, we find $e_r \approx 1\%$ *i.e.* a precision of $e_r = 0.005$ in absolute value. The effective diffusion coefficients follow the relation, with a slight difference (at most 10%) between the effective diffusion coefficients:

$$D_e^S > D_e^C > D_e^P > D_e^R \tag{22}$$

Although small, the differences between any of the estimates D_e^S, D_e^C, D_e^P and D_e^R is always larger than the relative error of 1%.

2.4 Relation Porosity-Tortuosity on Random Models

The tortuosity factors of random models are estimated by Equation (2). The molecule size effects and the viscous drag

TABLE 3

Diffusion coefficient from NMR measurements.

Sample	D_e^{NMR} 10^{-9} m^2/s	D_0^{NMR} 10^{-9} m^2/s	$\tau = K_d \frac{D_0^{NMR}}{D_e^{NMR}}$	$D_e = \varepsilon_t D_0 \frac{D_e^{NMR}}{D_0^{NMR}}$ 10^{-9} m^2/s	$F = \frac{D_0}{D_e}$
Toluene	2.40	2.40	1.00	2.40	1.00
Sample 1	1.52	2.36	1.47	1.05	2.29
Sample 2	1.57	2.60	1.57	1.01	2.38
Sample 3	1.40	2.24	1.52	1.08	2.22

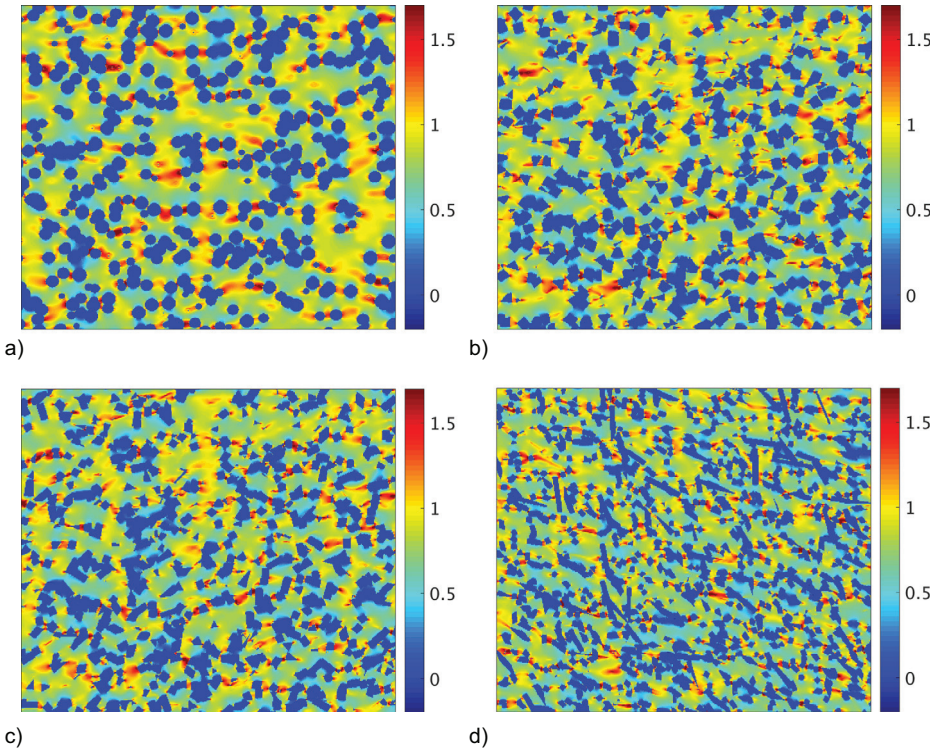

Figure 6

2D sections of the first component of the flux field J_1, obtained by FFT method on the Boolean models, with macroscopic concentration gradient $\langle -\nabla c \rangle$ = (1, 0, 0), with convergence criteria L1-norms difference of **E** between two iterations less than 10^{-6}. The microstructure volume is $300 \times 300 \times 300$ nm^3 (909^3 voxels at resolution 0.33 nm per voxel). The same macroscopic concentration gradient and the same convergence criteria are applied for all remaining computations of this work. a) sphere, b) cubic prism, c) platelet-like prism, d) rod-like prism.

TABLE 4

Parameters of the Boolean models of nano-particles (prism and sphere). The sphere radius is 2.5 nm The last column D_e is the effective diffusion coefficients of the Boolean models estimated with the numerical FFT method.

Particle shape	Pore volume fraction	Platelet shape (nm)				Effective diffusion
	ε	D_1	D_2	D_3	D_4	D_e
Sphere	0.7					0.566
Cubic prism	0.7	3.9	0.1	3.9	4.0	0.540
Platelet-like prism	0.7	7.0	0.1	2.9	3.0	0.533
Rod-like prism	0.7	1.9	0.1	1.9	16.0	0.518

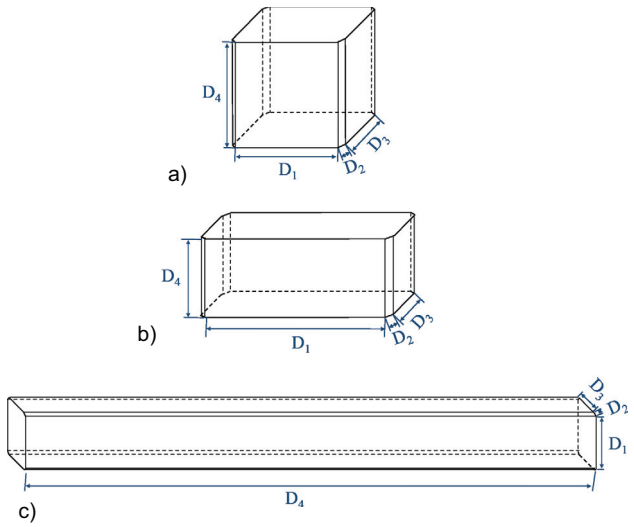

Figure 7

Prism shapes used in Section 2.3. The four parameters D_i, $i = 1$, 2, 3, 4 of the shapes are shown in Table 4. a) Cubic prism, b) platelet-like prism, c) rod-like prism.

effects are neglected in this subsection, so $K_p = K_d = 1$. $D(\mathbf{r})$ is set equal to $D_0 = 1$ in the pore space and $D_S = 0$ in the solid part. The tortuosity factor is then estimated by:

$$\tau = \frac{\varepsilon}{D_e} \tag{23}$$

Analytically, the self-consistent homogenization model provides a relationship between the pore volume fraction ε and the effective diffusion coefficient D_e [60, 61]:

$$\varepsilon \frac{D_0 - D_e}{\frac{1}{d}D_0 + \left(1 - \frac{1}{d}\right)D_e} + (1 - \varepsilon)\frac{D_s - D_e}{\frac{1}{d}D_s + \left(1 - \frac{1}{d}\right)D_e} = 0 \tag{24}$$

where d is the dimension factor (fixed at 3 in our case), D_s is the diffusion coefficient in the solid phase (fixed at 0 for alumina grains). Accordingly, we get $D_e = (3\varepsilon - 1)/2$, and the tortuosity factor is obtained by:

$$\tau = \frac{2\varepsilon}{3\varepsilon - 1}. \tag{25}$$

The relation between the pore volume fraction and the tortuosity factor (as indicated in Eq. 6) is studied on the four random models ((i)-(iv)) of increasing pore volume fractions:

(i) Boolean model of spheres;
(ii) Boolean model of isotropic platelets (platelet-like prisms);
(iii) Two-scale model of aligned platelets;
(iv) Two-scale model of aligned and aggregated platelets.

The platelets' size and shape are identified with the method presented in Section 1.1, and shown in Table 5.

The two-scale models of platelets are used to study the effects of platelet alignment and platelet aggregation on the effective diffusion coefficient and on the tortuosity factor. The platelet alignment is controlled by the parameters p_S and r_S. The platelet aggregation is controlled by the parameter p_A. When $p_A > 1 - \varepsilon > p_B$, the aligned platelets are considered to be aggregated, compared to isotropic platelets.

For the two-scale model (iii), the platelet density inside the aggregates is set as the overall solid volume fraction:

$$p_A = 1 - \varepsilon \tag{26}$$

The volume of spherical alignment zone is set to half of the overall volume:

$$p_S = 0.5 \tag{27}$$

TABLE 5

Parameters of the random models used in Sections 2.4 and 2.5. The coefficient p of Equation (6) is obtained by curve fitting for each model. The two-scale model of platelets (last row) is identified with the TEM images of sample 1 with the method presented in Section 1.1.

Platelets organization	ε	Platelets (nm)				Aggregates				
		D_1	D_2	D_3	D_4	p_A	p_S	r_S (nm)	p	Figure
Sphere	0.1–0.9								0.61	Figure 7a
Isotropic	0.1–0.9	14.3	2.4	2.0	3.3	0	0	0	0.83	Figure 7c
Aligned	0.1–0.9	14.3	2.4	2.0	3.3	$1 - \varepsilon$	0.5	30	0.86	Figure 10a
Aligned and aggregated	0.1–0.9	14.3	2.4	2.0	3.3	$1 - \varepsilon^2$	$0.5/(1 + \varepsilon)$	30	0.90	Figure 10b
Identified	0.69	14.3	2.4	2.0	3.3	0.3	0.2	30		Figure 11

For a fixed ε, the model (iii) is determined by Equations (10), (26) and (27). In this microstructure, half of the platelets are aligned, but not aggregated. The other half has isotropic orientations.

For the two-scale model (iv), the aggregation effect is added by setting:

$$p_A = 1 - \varepsilon^2 \tag{28}$$

which ensures $1 > p_A > 1 - \varepsilon > p_B > 0$. The volume fraction of aligned platelets $p_S p_A$ is set as:

$$p_S p_A = \frac{1 - \varepsilon}{2} \tag{29}$$

which means that half of the platelets are aligned. For a fixed ε, the model (iv) is determined by Equations (10), (28) and (29). The parameters of the random models of platelets are shown in Table 5.

The effective diffusion coefficients of the above four models are estimated with the FFT method, and shown in Figure 8. The effective diffusion coefficients are below the Hashin-Shtrikman upper bound. Compared to the Boolean model of spheres, the random model of platelets have slightly lower diffusion coefficients. This difference is more visible on the plot of tortuosity in Figure 9, the tortuosity being lower for the Boolean model of spheres.

The value of p in Equation (6) is estimated by curve fitting using least squares with $\varepsilon \geq 0.8$, and is shown in Table 5. The estimated tortuosity factors satisfy the Weissberg's lower bound ($p = 0.5$) for the Boolean model of spheres ($p = 0.61$).

As shown in Figures 8 and 9, the platelet alignment decreases the diffusivity and increases the tortuosity, compared to the isotropic platelets. At high pore volume fraction (*e.g.* $\varepsilon > 0.7$), the platelet aggregation has little influence on the diffusivity and the tortuosity factor, the pore volume fraction dominating the effective diffusion coefficient. At low porosity, like $\varepsilon = 0.3$, the aggregation helps to increase the effective diffusion coefficient. This is because the aggregation enlarges the pores outside the aggregates. The effect is shown in Figure 10.

In summary, at fixed pore volume fraction 0.7, without considering partition effects and drag effects, the effective diffusion coefficients of Boolean model of spheres (denoted by D_e^S), Boolean model of platelets (denoted by D_e^P), two-scale model of aligned platelets (denoted by D_e^{AP}) and two-scale model of aligned and aggregated platelets (denoted by D_e^{AAP}) satisfy the following inequalities, with weak differences (Tab. 6):

$$D_e^S > D_e^P > D_e^{AP} > D_e^{AAP} \tag{30}$$

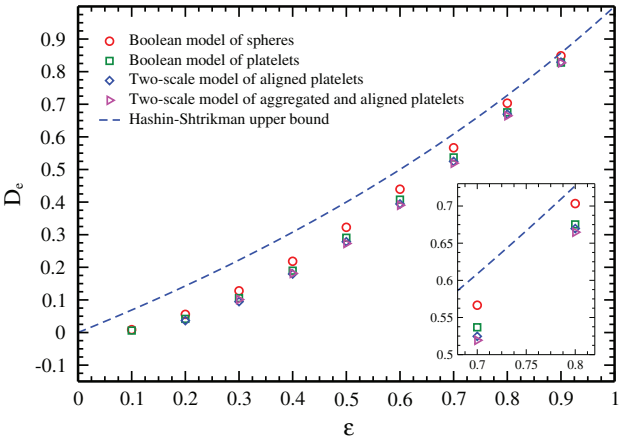

Figure 8

Effective diffusion coefficients D_e of random models, as a function of pore volume fraction ε.

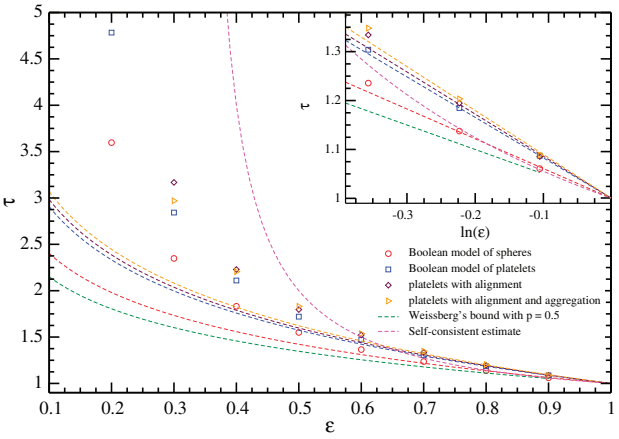

Figure 9

Tortuosity factor τ *versus* pore volume fraction ε of the random models in Section 2.4. The symbols (circle, square, diamond and triangle) are numerically estimated with the FFT method. The estimate by Equation (6) with Weissberg's bound $p = 0.5$ is plotted in green dotted curve. The estimate by the self-consistent method by Equation (25) is plotted in magenta dotted curve. The curve fittings with Equation (6) are performed with the data τ ($\varepsilon \geq 0.8$), and are plotted in dotted curves in the same color as the symbols (subplot). The corresponding values of p are shown in Table 5.

Once again,the relative error made on D_e^S, D_e^P, D_e^{AP} andD_e^{AAP} are found to be about 1%. The differences between the various estimates are also larger than the relative errors.

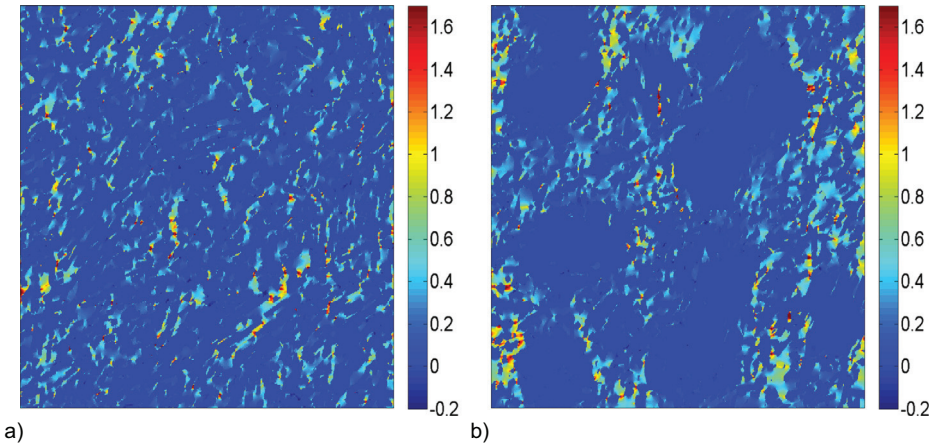

Figure 10

2D sections of the first component of the flux field J_1, with macroscopic concentration gradient $\langle -\nabla c \rangle = (1, 0, 0)$, obtained by FFT method on the two-scale models (iii) and (iv) used in Section 2.4 at $\varepsilon = 0.3$. The microstructure volume is $300 \times 300 \times 300$ nm^3 (909^3 voxels at resolution 0.33 nm per voxel). a) Aligned platelets, b) aligned and aggregated platelets.

2.5 Effective Diffusion of Identified Alumina Models

The two-scale model of platelets identified with the TEM images of sample 1 with the method presented in Section 1.1 is considered. The parameters of the model are shown in Table 5 (last row).

The volume of the microstructures are 300^3 nm^3, with resolution 0.33 nm per voxel. The global pore volume fraction is set to 0.69 (the same as sample 1). A concentration gradient is imposed between the two faces along the $\mathbf{e}_1$ axis: $\bar{\mathbf{E}} = (1, 0, 0)$. The diffusion flux and effective properties are computed by averaging the field $J_1(\mathbf{r})$ numerically estimated by the FFT method. A map of the local flux field $J_1(\mathbf{r})$ is shown in Figure 11. Results for the effective properties are given in Table 6 and compared with the models defined in Section 2.4.

In the numerical computation of Fick's diffusion, the hindering effects (the drag effect and the partition effect caused by molecule size) are neglected. Without hindering effects taken into account, the estimated formation factor is about 15% lower than the NMR measurements ($F = 1.96$ compared to $F = 2.29$), as shown in Table 7.

Approximatively, we use Equations (4) and (3) to compensate the hindering effect:

$$D'_e = K_p K_d D_e \tag{31}$$

The formation factor $F' = \frac{D_0}{D'_e}$ is then estimated, and shown in the column F' in Table 7. The formation factors of the two-scale model ($F' = 2.19$) is closer to the NMR measurement result ($F = 2.29$), with a 4.4% relative error.

TABLE 6

Comparison between the effective diffusion coefficients numerically estimated on the random models with different particle morphologies. The parameters of the models are shown in Table 5. The absolute error on the predicted effective diffusion coefficient of the two-scale model of platelets is about 0.005 (Sect. 2.4).

Platelet organization	ε	D_e
Sphere	0.7	0.566
Isotropic	0.7	0.537
Aligned	0.7	0.525
Aligned and aggregated	0.7	0.519
Identified	0.69	0.508

2.6 Modeling of Hindered Diffusion

The compensation of the partition effect by Equations (3) and (31) is based on a cylindrical pore assumption, which is a rough approximation. To model the hindering effect of molecule size with a better precision, we change the pores by morphological dilation of the solid phase with spherical structuring elements. The radii of spherical structuring elements are equal to the gyration radii of molecules. It increases up to reach the percolation threshold. Such dilations are performed accurately and efficiently from the distance transform of the model.

The modeling is performed on a microstructure simulated from the identified two-scale model of platelets, with parameters shown in Table 5. The volume of the microstructure is 322^3 nm^3, with voxel's side length 0.35 nm.

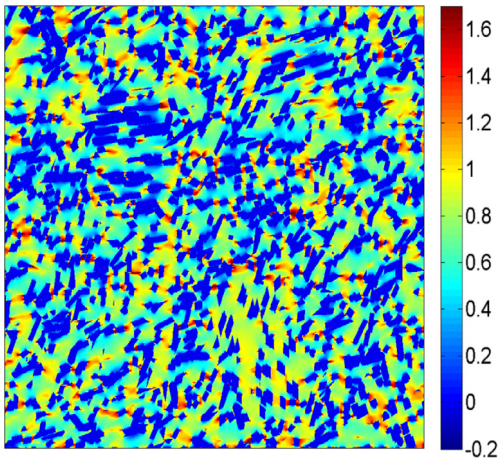

Figure 11

2D section of the first component of the flux field J_1, with macroscopic concentration gradient $\langle -\nabla c \rangle = (1, 0, 0)$, obtained by FFT method on the identified random model of platelets with parameters shown in Table 5. The microstructure volume is $300 \times 300 \times 300$ nm^3 (909^3 voxels at resolution 0.33 nm per voxel).

Dilations are performed on the microstructure with gyration radius r_g from 0.35 nm to 3.5 nm.

The flux field of Fick's diffusion is computed using the FFT method, with a macroscopic concentration gradient applied along axis $\mathbf{e}_1$. Some 2D sections of the first component of the flux fields are presented in Figure 12. The effective diffusion coefficients as function of gyration radius, denoted by $D_e(r_g)$, are estimated and shown in Figure 13. The larger the molecule, the lower the effective diffusion coefficient. The effective diffusion coefficient tends to zero when the pore percolation threshold is approached. Molecules of gyration radius larger than 3.5 nm cannot be transported by diffusion in the alumina model. The estimates are compared with the cylindrical-pore approximation by Equation (3), presented by blue dotted curve in Figure 13.

The tortuosity factor of the microstructure differs for molecules of different gyration radius, because of different accessible pore volume fraction. The tortuosity factor as function of accessible pore volume fraction is plotted in Figure 14, compared with an experimental reference by Inverse Size Exclusion Chromatography (ISEC) with $p = 2.4$ [5] plotted in blue dotted curve.

To estimate the partition effect of toluene molecules, the microstructure is upsampled by a factor 2 to achieve a better resolution. After numerical computation, an extra point near $r_g = 0.16$ nm is obtained in Figure 13. The effective diffusion coefficient with partition effect taken into account, denoted by D''_e, is estimated by:

$$D''_e = K_d D_e(r_g) \tag{32}$$

where the drag effect coefficient K_d is still approximated by Equation (4). The formation factor of the identified two-scale model for toluene is estimated ($F'' = 2.34$), which is 2% higher than the NMR measurements on sample 1 ($F = 2.29$), as shown in Table 7, showing an excellent agreement.

3 DISCUSSION

T_1 and T_2 values obtained for free toluene molecules are in agreement (about 2) with those observed in the literature at high field NMR [62] (Tab. 2).

T_1/T_2 ratio is found higher for confined toluene molecules due to stronger interactions with alumina surface. As a first consequence of toluene – surface interactions, spectral contributions (NMR ^{1}H) are broadened in presence of alumina extrudates. More in details, we may observe a doublet in the aromatic and aliphatic regions at lower chemical shift (Fig. 4). Indeed toluene molecules confined in the porous network experience a lower magnetic field than those present outside of the extrudate. Since molecular exchange between the two domains (inner

TABLE 7

Comparison of effective diffusion coefficients and tortuosity factors between numerical computation and NMR measurements on sample 1. For the sample 1, the D_e and D_0 are respectively the diffusion coefficient of confined and free toluene measured by NMR. For the two-scale model, D_e and $D_e(r_g)$ are numerically estimated with the FFT method. D'_e is the effective diffusion coefficient compensated with the cylindrical-pore approximation by Equation (31). D''_e is the effective diffusion coefficient compensated with the partition effect by dilation, by Equation (32). τ' and τ'' are respectively the corresponding tortuosity factors calculated from D'_e and D''_e.

Microstructure	D_e 10^{-9} m^2/s	D_0 10^{-9} m^2/s	$F = \frac{D_0}{D_e}$	D'_e 10^{-9} m^2/s	$F' = \frac{D_0}{D'_e}$	$D_0(r_g)$ 10^{-9} m^2/s	D''_e 10^{-9} m^2/s	$F'' = \frac{D_0}{D''_e}$
Sample 1	1.05	2.40	**2.29**					
Two-scale model	0.508	1	1.96	0.46	2.19	0.453	0.427	**2.34**

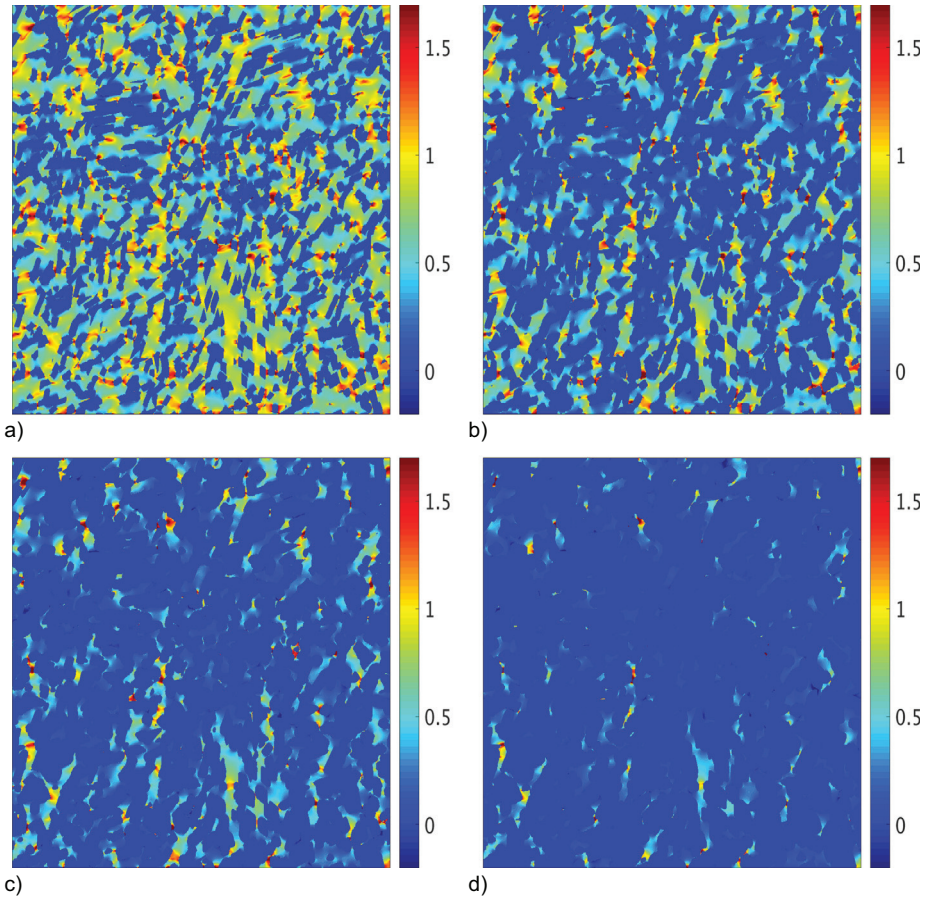

Figure 12

2D sections of the first component of the flux field J_1 of molecules of increasing gyration radius, with macroscopic concentration gradient $\langle -\nabla c \rangle = (1, 0, 0)$, computed by FFT method on the identified two-scale model of platelets with parameters shown in Table 5. The microstructure volume is $300 \times 300 \times 300$ nm^3 (909^3 voxels at resolution 0.33 nm per voxel). a) $r_g = 0.35$ nm, b) $r_g = 1.06$ nm, c) $r_g = 1.77$ nm, d) $r_g = 2.49$ nm.

and outer sides of the extrudates) is limited at 295 K and for 140 ms diffusion time, two distinct spectral contributions are observed in the NMR spectra. It is nevertheless important to notice that toluene molecules outside of the pores report a T_2 value below that of free molecules (Tab. 2). It may indicate that all toluene molecules present in the NMR tube are impacted or perturbed by the presence of alumina extrudates and cannot be considered as "totally" free molecules. This observation may also partly explain the differences observed in D_0^{NMR}value (2.24 to 2.60 $\times$ 10^{-9} m^2/s) for the three alumina samples which was at first expected to be independent of the studied sample (Tab. 3).

Effective diffusion coefficients of the three alumina determined from DOSY experiments are pretty close in agreement with their relatively close textural properties.

For catalyst support formed by nano-particles, spherical or cubic grains are slightly more favorable than elongated grains, in terms of effective diffusion property.

For small molecules, the platelet aggregation has opposite effects on the diffusion property at low and at high pore volume fraction. Since the refining industry has more interest in catalyst supports of high pore volume fraction (*e.g.* $\varepsilon > 0.6$), platelet alignment and aggregation do not increase the diffusion coefficient.

For large molecules, for which the hindering effect is strong, the platelet alignment and aggregation change the pore size distribution, and thus increase the diffusion coefficient. The study in Section 2.4 shows that aggregation helps to enlarge the pore size outside the aggregates, and is favorable for the diffusion. However, this part remains to be checked for the entire curve in Figure 13. By now, only the effective diffusion coefficient of toluene has been confirmed by PFG-NMR. In fact, the property $D_e(r_g)$ is a descriptor of the pore size distribution of a catalyst support.

In the model identification and the numerical computations of diffusion flux, only the measurements on sample 1

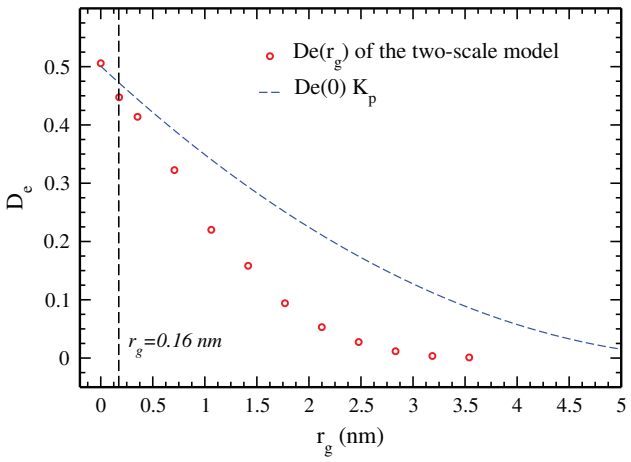

Figure 13

Effective diffusion coefficient D_e of the two-scale model of platelets as a function of increasing gyration radius of molecules r_g. The parameters of the two-scale model are shown in Table 5. The gyration radius of toluene is marked in vertical dotted curve. The approximation of the partition effect by Equation (3) is presented in blue dotted curve.

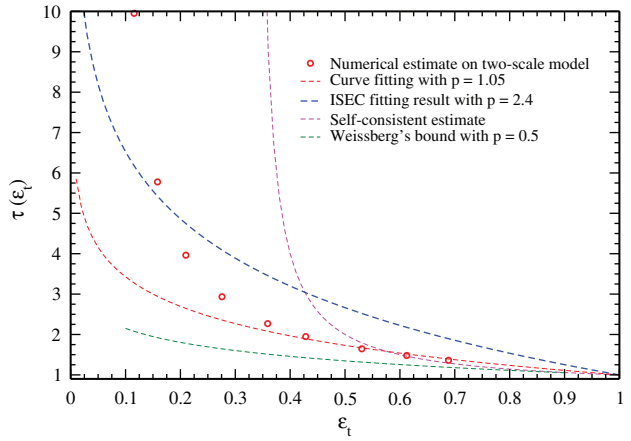

Figure 14

Tortuosity factor τ *versus* accessible pore volume fraction ε_t in hindered diffusion. The accessible pore volume fractions ε_t are numerically measured on microstructures after dilation of size r_g. The tortuosity factors are estimated with Equation (23) and corresponding effective diffusion coefficients shown in Figure 13. The red dotted curve is obtained by curve fitting using Equation (6), with the points in $\varepsilon_t > 0.4$.

were used as experimental reference. This is because the three samples of γ-alumina have very close textures. The information extracted from NMR, nitrogen porosimetry and TEM images (not shown) is not precise enough to differentiate the three samples. A finer model, or samples of distinct textures are among the perspectives of this work.

CONCLUSION

In this work, the hindered diffusion in mesoporous alumina was measured by PFG-NMR and numerically studied with the FFT-diffusion method. The effective diffusion coefficients (D_e) of Boolean models of different shapes were estimated. At a fixed pore volume fraction $\varepsilon = 0.7$, Boolean model of spheres has slightly higher D_e than cubic prisms, while the latter has slightly higher D_e than platelet-like and rod-like platelets.

The formation factors were estimated as the ratio of free and confined diffusion coefficients. The relation between the pore volume fraction and the tortuosity were studied on random models of spheres and platelets of increasing ε. Spherical grains produce higher D_e than platelets at all pore volume fractions between 0.1 and 0.9. At low pore volume fractions ($\varepsilon < 0.5$), the platelet aggregation increases the diffusion coefficient. At high pore volume fractions ($\varepsilon > 0.5$), the platelet alignment and aggregation both decrease the diffusion coefficient and increase the tortuosity factor.

The effective diffusion coefficient and the formation factors of the two-scale model of platelets, identified with TEM images of sample 1, were estimated. The partition effect caused by the molecule gyration radius (r_g) was modeled by a dilation operation of the solid phase. The effective diffusion coefficients of the two-scale model as function of molecule size were obtained. The formation factor of the identified two-scale model of γ-alumina for toluene (2.34) is close to the RMN measurement (2.29), with a 2% relative error.

REFERENCES

1 Merdrignac I., Roy-Auberger M., Guillaume D., Verstraete J. (2013) Hydroprocessing and hydroconversion of residue fractions, in: Toulhoat H., Raybaud P. (eds), *Catalysis by Transition Metal Sulfides*, Editions TECHNIP, Paris, France.

2 Iglesia E., Soled S., Baumgartner J., Reyes S. (1995) Synthesis and catalytic properties of eggshell cobalt catalysts for the Fischer-Tropsch synthesis, *Journal of Catalysis* **153**, 1, 108-122.

3 Derrien M. (1986) Selective hydrogenation applied to the refining of petrochemical raw materials produced by steam cracking, *Studies in Surface Science and Catalysis* **27**, 613-666.

4 Godinez C., Cabanes A., Villora G. (1995) Experimental study of the front-end selective hydrogenation of steam-cracking C_2-C_3 mixture, *Chemical Engineering and Processing: Process Intensification* **34**, 5, 459-468.

5 Wernert V., Bouchet R., Denoyel R. (2010) Influence of molecule size on its transport properties through a porous medium, *Analytical Chemistry* **82**, 7, 2668-2679.

6 Deen W. (1987) Hindered transport of large molecules in liquid-filled pores, *AIChE Journal* **33**, 9, 1409-1425.

7 Dechadilok P., Deen W. (2006) Hindrance factors for diffusion and convection in pores, *Industrial & Engineering Chemistry Research* **45**, 21, 6953-6959.

8 Satterfield C., Colton C., Pitcher W. (1973) Restricted diffusion in liquids within fine pores, *AIChE Journal* **19**, 3, 628-635.

9 Comiti J., Renaud M. (1989) A new model for determining mean structure parameters of fixed beds from pressure drop measurements: application to beds packed with parallelepipedal particles, *Chemical Engineering Science* **44**, 7, 1539-1545.

10 Weissberg H. (1963) Effective diffusion coefficient in porous media, *Journal of Applied Physics* **34**, 9, 2636-2639.

11 Barrande M., Bouchet R., Denoyel R. (2007) Tortuosity of porous particles, *Analytical Chemistry* **79**, 23, 9115-9121.

12 Hollewand M., Gladden L. (1995) Transport heterogeneity in porous pellets – I. PGSE NMR studies, *Chemical Engineering Science* **50**, 2, 309-326.

13 Prasher B., Ma Y.H. (1977) Liquid diffusion in microporous alumina pellets, *AIChE Journal* **23**, 3, 303-311.

14 Tayakout M., Ferreira C., Espinat D., Arribas Picon S., Sorbier L., Guillaume D., Guibard I. (2010) Diffusion of asphaltene molecules through the pore structure of hydroconversion catalysts, *Chemical Engineering Science* **65**, 5, 1571-1583.

15 Callaghan P., MacGowan D., Packer K., Zelaya F. (1990) High-resolution q-space imaging in porous structures, *Journal of Magnetic Resonance* **90**, 1, 177-182.

16 Tanner J. (1970) Use of the stimulated echo in NMR diffusion studies, *The Journal of Chemical Physics* **52**, 5, 2523-2526.

17 Valiullin R., Kärger J. (2011) The impact of mesopores on mass transfer in nanoporous materials: evidence of diffusion measurement by NMR, *Chemie Ingenieur Technik* **83**, 1-2, 166-176.

18 Wood J., Gladden L. (2003) Effect of coke deposition upon pore structure and self-diffusion in deactivated industrial hydroprocessing catalysts, *Applied Catalysis A: General* **249**, 2, 241-253.

19 Kortunov P., Vasenkov S., Kärger J., Valiullin R., Gottschalk P., Fé Elía M., Perez M., Stöcker M., Drescher B., McElhiney G., Berger C., Gläser R., Weitkamp J. (2005) The role of mesopores in intracrystalline transport in USY zeolite: PFG NMR diffusion study on various length scales, *Journal of the American Chemical Society* **127**, 37, 13055-13059.

20 Kirchner T., Shakhov A., Zeigermann P., Valiullin R., Kärger J. (2012) Probing mesopore connectivity in hierarchical nanoporous materials, *Carbon* **50**, 13, 4804-4808.

21 Morris K.F., Johnson C.S. Jr (1992) Diffusion-ordered two-dimensional nuclear magnetic resonance spectroscopy, *Journal of the American Chemical Society* **114**, 8, 3139-3141.

22 Johnson C.S. (1999) Diffusion ordered nuclear magnetic resonance spectroscopy: principles and applications, *Progress in Nuclear Magnetic Resonance Spectroscopy* **34**, 3, 203-256.

23 Morris G.A. (2002) *Diffusion-Ordered Spectroscopy (DOSY)*, pp. 35-44.

24 Ernst R.R. (1992) Nuclear magnetic resonance Fourier transform spectroscopy (Nobel lecture), *Angewandte Chemie International Edition in English* **31**, 7, 805-823.

25 Durand E., Clemancey M., Quoineaud A.-A., Verstraete J., Espinat D., Lancelin J.-M. (2008) ^{1}H diffusion-ordered spectroscopy (DOSY) nuclear magnetic resonance (NMR) as a powerful tool for the analysis of hydrocarbon mixtures and asphaltenes, *Energy & Fuels* **22**, 4, 2604-2610.

26 Krüger G., Weiss R. (1970) Diffusionskonstanten einiger organischer Flüssigkeiten, *Zeitschrift für Naturforschung A* **25**, 5, 777-780.

27 Harris K., Alexander J., Goscinska T., Malhotra R., Woolf L., Dymond J. (1993) Temperature and density dependence of the selfdiffusion coefficients of liquid *n*-octane and toluene, *Molecular Physics* **78**, 1, 235-248.

28 Pickup S., Blum F. (1989) Self-diffusion of toluene in polystyrene solutions, *Macromolecules* **22**, 10, 3961-3968.

29 Santos F., Nieto de Castro C., Dymond J., Dalaouti N., Assael M., Nagashima A. (2006) Standard reference data for the viscosity of toluene, *Journal of Physical and Chemical Reference Data* **35**, 1, 1-8.

30 Sahimi M. (1993) Flow phenomena in rocks: from continuum models to fractals, percolation, cellular automata, and simulated annealing, *Reviews of Modern Physics* **65**, 4, 1393-1534.

31 Kosek J., Stepanek F., Marek M. (2005) Modeling of transport and transformation processes in porous and multiphase bodies, in *Multiscale Analysis in Advances in Chemical Engineering*, G. Marin (ed.), Elsevier, pp. 137-203.

32 Reyes S., Iglesia E. (1991) Effective diffusivities in catalyst pellets: new model porous structures and transport simulation techniques, *Journal of Catalysis* **129**, 2, 457-472.

33 Štěpánek F., Ansari M.A. (2005) Computer simulation of granule microstructure formation, *Chemical Engineering Science* **60**, 14, 4019-4029.

34 Koci P., Novak V., Stepanek F., Marek M., Kubicek M. (2010) Multi-scale modelling of reaction and transport in porous catalysts, *Chemical Engineering Science* **65**, 1, 412-419. *20th International Symposium on Chemical Reaction Engineering – Green Chemical Reaction Engineering for a Sustainable Future*, 7-10 September, Kyoto, Japan.

35 Yeong C., Torquato S. (1998) Reconstructing random media, *Physical Review E* **57**, 1, 495-506.

36 Rozman M., Utz M. (2001) Efficient reconstruction of multiphase morphologies from correlation functions, *Physical Review E* **63**, 6, 066701.

37 Jeulin D. (2012) Morphology and effective properties of multi-scale random sets: a review, *Comptes Rendus Mécanique* **340**, 4-5, 219-229.

38 Adler P., Jacquin C., Quiblier J. (1990) Flow in simulated porous-media, *International Journal of Multiphase Flow* **16**, 4, 691-712.

39 Diaz I., Gonzalez-Pena V., Marquez-Alvarez C., Kikkinides E. (2004) Transmission electron microscopy combined with stochastic reconstruction methods for structural characterization of porous alumina synthesized via non-ionic surfactant-templating route, *Microporous and Mesoporous Materials* **68**, 1-3, 11-19.

40 Koci P., Stepanek F., Kubicek M., Marek M. (2006) Meso-scale modelling of CO oxidation in digitally reconstructed porous Pt/gamma-Al_2O_3 catalyst, *Chemical Engineering Science* **61**, 10, 3240-3249.

41 Youssef S., Rosenberg E., Gland N., Kenter J., Skalinski M., Vizika O. (2007) High resolution CT and pore-network models to assess petrophysical properties of homogeneous and heterogeneous carbonates, in *SPE/EAGE Reservoir Characterization and Simulation Conference*.

42 Rigby S., Gladden L. (1999) The prediction of transport properties of porous media using fractal models and NMR experimental techniques, *Chemical Engineering Science* **54**, 15-16, 3503-3512, *15th International Symposium on Chemical Reaction Engineering (ISCRE 15)*, 13-16 September, 1998, Newport Beach, CA.

43 Euzen P., Raybaud P., Krokidis X., Toulhoat H., Le Loarer J.-L., Jolivet J.-P., Froidefond C. (2002) Alumina, in *Handbook of porous solids*, F. Schüth, K. Sing, J. Weitkamp (eds), Wiley-VCH, Weinheim, pp. 1591-1677.

44 Digne M., Sautet P., Raybaud P., Euzen P., Toulhoat H. (2004) Use of DFT to achieve a rational understanding of acid-basic properties of γ-alumina surfaces, *Journal of Catalysis* **226**, 1, 54-68.

45 Chiche D., Digne M., Revel R., Chanéac C., Jolivet J.-P. (2008) Accurate determination of oxide nanoparticle size and shape based on X-ray powder pattern simulation: application to boehmite AlOOH, *The Journal of Physical Chemistry C* **112**, 23, 8524-8533.

46 Rozita Y., Brydson R., Comyn T., Scott A., Hammond C., Brown A., Chauruka S., Hassanpour A., Young N., Kirkland A., Sawada H., Smith R. (2013) A Study of Commercial Nanoparticulate γ-Al_2O_3 Catalyst Supports, *ChemCatChem* **5**, 9, 2695-2706.

47 Klimov O., Leonova K., Koryakina G., Gerasimov E., Prosvirin I., Cherepanova S., Budukva S., Pereyma V., Dik P., Parakhin O., Noskov A. (2014) Supported on alumina Co-Mo hydrotreating catalysts: Dependence of catalytic and strength characteristics on the initial AlOOH particle morphology, *Catalysis Today* **220**, 66-77.

48 Pardo P., Montoya N., Alarcón J. (2015) Tuning the size and shape of nano-boehmites by a free-additive hydrothermal method, *CrystEngComm* **17**, 10, 2091-2100.

49 Lee J., Jeon H., Oh D., Szanyi J., Kwak J. (2015) Morphology-dependent phase transformation of γ-Al_2O_3, *Applied Catalysis A: General* **500**, 58-68.

50 Moreaud M., Jeulin D., Morard V., Revel R. (2012) TEM image analysis and modelling: application to boehmite nanoparticles, *Journal of Microscopy* **245**, 2, 186-199.

51 Wang H., Pietrasanta A., Jeulin D., Willot F., Faessel M., Sorbier L., Moreaud M. (2015) Modelling mesoporous alumina microstructure with 3D random models of platelets, *Journal of Microscopy* **260**, 3, 287-301.

52 Mu D., Liu Z.-S., Huang C., Djilali N. (2007) Prediction of the effective diffusion coefficient in random porous media using the finite element method, *Journal of Porous Materials* **14**, 1, 49-54.

53 Moulinec H., Suquet P. (1994) A fast numerical method for computing the linear and nonlinear mechanical properties of composites, *Comptes rendus de l'Académie des sciences. Série II, Mécanique, physique, chimie, astronomie* **318**, 11, 1417-1423.

54 Willot F., Abdallah B., Pellegrini Y.-P. (2014) Fourier-based schemes with modified Green operator for computing the electrical response of heterogeneous media with accurate local fields, *International Journal for Numerical Methods in Engineering* **98**, 7, 518-533.

55 Hashin Z., Shtrikman S. (1963) A variational approach to the theory of the elastic behaviour of multiphase materials, *Journal of the Mechanics and Physics of Solids* **11**, 2, 127-140.

56 Brunauer S., Emmett P., Teller E. (1938) Adsorption of gases in multimolecular layers, *Journal of the American Chemical Society* **60**, 2, 309-319.

57 Wu D.H., Chen A.D., Johnson C.S. (1995) An improved diffusion-ordered spectroscopy experiment incorporating bipolar-gradient pulses, *Journal of Magnetic Resonance, Series A* **115**, 2, 260-264.

58 Archie G.E. (1942) The electrical resistivity log as an aid in determining some reservoir characteristics, *Transactions of the AIME* **146**, 01, 54-62.

59 Titze T., Lauerer A., Heinke L., Chmelik C., Zimmermann N. E., Keil F.J., Ruthven D.M., Kärger J. (2015) Transport in nanoporous materials including MOFs: The applicability of Fick's laws, *Angewandte Chemie International Edition* **54**, 48, 14580-14583.

60 Bruggeman D.A.G. (1935) Calculation of various physics constants in heterogenous substances I dielectricity constants and conductivity of mixed bodies from isotropic substances, *Annals of Physics* **24**, 7, 636-664.

61 Kanaun S.K., Levin V. (2003) *Self-Consistent Methods for Composites: Vol. 1 – Static Problems*, Springer, Dordrecht.

62 D'Agostino C., Chansai S., Bush I., Gao C., Mantle M.D., Hardacre C., James S.L., Gladden L.F. (2016) Assessing the effect of reducing agents on the selective catalytic reduction of NO_x over Ag/Al_2O_3 catalysts, *Catalysis Science & Technology* **6**, 6, 1661-1666.

Manuscript submitted in October 2016
Manuscript accepted in January 2017
Published online in March 2017

Cite this article as: H. Wang, F. Willot, M. Moreaud, M. Rivallan, L. Sorbier and D. Jeulin (2017). Numerical Simulation of Hindered Diffusion in γ-Alumina Catalyst Supports, *Oil Gas Sci. Technol* **72**, 8.